Research Article

Mechanical Properties Evaluation and Crack Propagation Behavior in Dissimilar Metal Welded Joints of 304 L Austenitic Stainless Steel and SA508 Low-Alloy Steel

Yuman Sun [iD],[1] **He Xue** [iD],[1] **Fuqiang Yang** [iD],[2] **Shuai Wang** [iD],[1] **Shun Zhang,**[1] **Jinxuan He,**[1] **and Rehmat Bashir** [iD][1,3]

[1]*School of Mechanical Engineering, Xi'an University of Science and Technology, Xi'an 710054, China*
[2]*School of Science, Xi'an University of Science and Technology, Xi'an 710054, China*
[3]*Department of Mechanical Engineering, University of Engineering and Technology, Lahore 54890, Pakistan*

Correspondence should be addressed to Yuman Sun; 19205201061@stu.xust.edu.cn and He Xue; xuehe@xust.edu.cn

The material mechanical properties and crack propagation behavior of dissimilar metal welded joint (DMWJ) of pressurized water reactor (PWR) was investigated. In this research, the mechanical parameters of the cladding layer materials (304L-SA508) of the DMWJ in PWRs were obtained by the continuous indentation test. Simultaneously, the user-defined (USDFLD) subroutine in ABAQUS was used to establish the heterogeneous materials model of the welded joint. On this basis, the local crack propagation path of DMWJs has been discussed based on the extended finite element method (XFEM). The result indicated that the strength value at the fusion boundary line (FB line) is the largest, and the yield strength reaches 689 MPa. The yield stress values of the cladding metal (304 L) and base metal (SA508) are 371 MPa and 501 MPa, respectively. Affected by the material constraint effect of the DMWJ, the crack will propagate through the FB line when the initial crack is perpendicular to the FB line. And when the initial crack parallels the FB line, the crack will deviate from it. Meanwhile, the crack propagation length is smaller as the initial crack tip is closer to the FB line when the load condition is constant.

1. Introduction

Dissimilar metal welded joints (DMWJs) are widely used to connect different metal materials in many engineering structural components, such as reactor pressure vessels (RPV) and pipes [1–3]. Moreover, nickel-base alloys such as Alloy 152/52 M, Alloy 309 L/308 L, and Alloy 182/82 have been widely used as weld metals [4, 5]. During the welding and service process of such structures, flaws such as cracks may occur in DMWJs due to the influence of microstructure and mechanical property inhomogeneity. It is demonstrated in several experiences of nuclear power plants (NPPs) that the weld zone is more susceptible to stress corrosion cracking (SCC) caused by hydrochemistry, material, and mechanical factors, which seriously threatens the safe operation of in-service NPPs [6–10], as shown in Figure 1.

Therefore, it is great to assess structural integrity accurately for such DMWJs with cracks.

Accurately measuring the material mechanical properties of the critical components of the welded joint in the main pipeline of the in-service NPP is an effective means to ensure its safe operation. Several studies have demonstrated that the mechanical properties in the heat-affected zone (HAZ) of DMWJs become complex, which extremely affects the structural integrity of critical components in PWRs [11–13]. In addition, the material constraint effect of the DMWJ will lead to the uneven distribution of stress-strain conditions around the tip of the crack, which is one of the main factors affecting SCC [14–16]. In previous studies, some scholars have attempted to obtain the material mechanical properties of DMWJs by microhardness test or mini-sized tensile test [2, 17, 18], and the experiments in this

field have shown that the strength of the weld zone and HAZ has changed dramatically. Nevertheless, the welded joint needs to be sliced in different positions, releasing residual stress and changing mechanical properties of the welded joint. The continuous indentation test is known as the "probe of material mechanical properties," which can effectively characterize the material mechanical properties of metals and compound materials [19–22]. Xue et al. [20] carried out tensile work hardening and continuous indentation tests on nuclear-grade austenitic stainless steel (316 L). The results indicated that the deviation of yield strength and tensile strength obtained by the continuous indentation test is within the allowable error range. In this study, the mechanical properties such as yield strength σ_y and tensile strength σ_u of the cladding layer of the DMWJ in PWRs were obtained by the continuous indentation test.

More recently, several scholars have been devoted to understanding the mechanism of the crack propagation behavior in DMWJs to avoid the sudden fracture failure in the weld zone by SCC in PWRs [23–26]. Fan et al. [27, 28] investigated the effects of work hardening mismatch on fracture resistance behavior of cracks in bimaterial interface zone based on the Gurson–Tvergaard–Needleman ductile damage mechanics model. The results indicated that the work hardening mismatch influences the crack growth path. In addition, it is an effective means for the numerical simulation of the crack propagation behavior in DMWJs based on the extended finite element method (XFEM). Yang et al. [29] studied three-point bending specimens with the material mechanical properties mismatch by XFEM. The results illustrated that the specimens with larger ultimate tensile strength mismatch are prone to interface crack propagation. The effect of elastic modulus mismatch on crack propagation can be ignored. To date, little literature could be found on the crack propagation behavior of DMWJs with heterogeneous materials.

In this study, the local mechanical properties of the cladding layer of the DMWJ were obtained by continuous indentation test, and the heterogeneous material model of the DMWJ was established by the user-defined field (USDFLD) subroutine for numerical simulation test. Since then, the local crack propagation behavior in DMWJs has been discussed based on XFEM.

2. Continuous Indentation Test

As schematically shown in Figure 2, the pipe-nozzle material of the SA508-52M-316L DMWJ is low-alloy steel (SA508), and the safety end pipe material is austenitic stainless steel (316 L). The DMWJ is prepared by deposition a buttering layer on the surface of SA508 by gas tungsten arc welding (GTAW; 120–160 A, 10–12 V, 1.85 mm/s, and interpass temperature <203°C). Then a heat treatment (keep at 610°C for 15 h, then cool the furnace to 300°C) was conducted on the buttering to relieve the residual stress. By performing multilayer welding on GTAW, the buttering layer is connected to the safety end pipe, but the buttering layer and the multilayer is the nickel-base alloy (Alloy 52 M). To prevent corrosion of the inner surface of the pipe nozzle and local
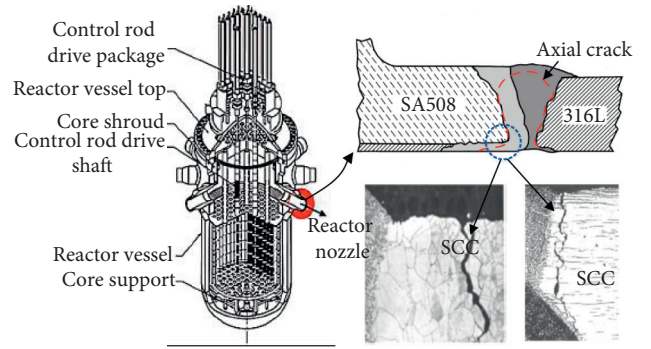

Figure 1: Schematic diagram of stress corrosion cracking of welded joint at the safety end of the primary circuit of PWRs [9, 10].
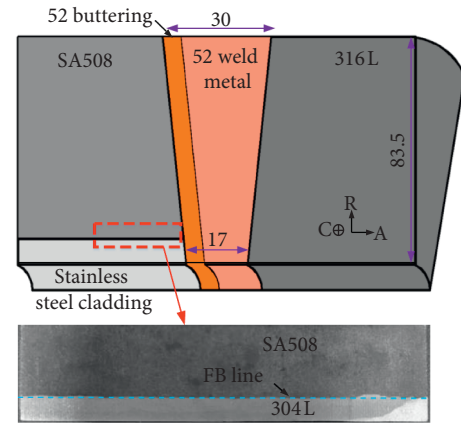

Figure 2: Stainless steel cladding layer specimen of welded joint of the pressure vessel (C, circumferential; R, radial direction; and A, axial direction).

welded joint, electrode arc welding is used to deposit a layer of austenitic stain steel (304 L) on its surface with a thickness of 8.5 mm. There is a fusion zone with a width of 0.02 mm~0.2 mm near the fusion boundary line (FB line) and a width of 2 mm~3 mm of HAZ on the side of the base metal [2, 7].

More recently, the continuous indentation test, widely used to obtain material mechanical properties [20–23], obtained the multicycle load-depth ($P - h$) curve by pressing the indenter vertically into the same test point on the surface of the metal specimen with a specific cyclic load. The elastic modulus E, yield strength σ_y, and tensile strength σ_u of the metal can be determined by transforming the multicycle load-depth ($P - h$) curves into the characteristic stress-strain ($\sigma - \varepsilon$) curves. Tabor et al. [30] have proposed that the characteristic stress σ_r of indentation was replaced by the ratio of load and contact region under the case of complete plastic deformation, and the calculation equation is as follows:

$$\sigma_r = \frac{1}{\Psi} \frac{F}{A} = \frac{1}{\Psi} \frac{F}{\pi a^2}, \tag{1}$$

where F is the indenter load value; a is the contact radius between the indenter and specimen when considering the deformation of the region around the indentation; Ψ is the

plastic constraint factor, which is related to the yield strain and strain hardening exponent n of the metal specimen; and $\Psi = 3$ was defined in NPR-ISO/TR 29381 [31, 32]. The characteristic stress ε_r of indentation was proposed by AHN [33] based on the concept of shear strain at the contact edge, which can be expressed as follows:

$$\varepsilon_r = \alpha \frac{1}{\sqrt{1 - (a/R)^2}} \frac{a}{R} = \alpha \tan \gamma, \qquad (2)$$

where $\tan \gamma$ is the shear strain of the contact edge and α is a constant independent of the metal specimen, which $\alpha = 0.14$ was defined in NPR-ISO/TR 29381 [32].

In this study, the array indentation test points were set at the welded joint to characterize the material mechanical properties of the base metal, weld zone, and HAZ of the welded joints, as shown in Figure 3. In order to avoid the influence of indentation interval on the measurement accuracy of the continuous indentation test, the interval between two columns of indentation test points was set to 1.25 mm, and the vertical interval was set to 1.5 mm. A total of six arrays were set up, and the data obtained from the test points in the same column were averaged. Dao et al. [34] characterized true stress-strain curve by improved elastic-plastic model, which is adapted to characterization the mechanical properties of DMWJs in PWRs; the equation is as follows:

$$\sigma = \begin{cases} E\varepsilon, & K\varepsilon^n, \\ \sigma \le \sigma_y, & \sigma > \sigma_y, \end{cases}$$
$$\sigma_y = E\varepsilon_y = K\varepsilon_y^n, \qquad (3)$$

where K is the strength factor and n is the strain hardening exponent. The improved elastic-plastic model based on the method of characterizing stress and strain is as follows:

$$\sigma_r = \sigma_y \left(1 + \frac{E}{\sigma_y} \varepsilon_r \right)^n. \qquad (4)$$

The tensile strength σ_u is the maximum value in the engineering stress-strain curve. The derivation of engineering stress can be derived as $n = \ln(1 + \varepsilon_e) = \varepsilon$, when $\varepsilon = n$, the tensile strength.

$$\sigma_u = K \left(\frac{n}{e} \right)^n, \qquad (5)$$

where e is the natural index.

According to equations (4) and (5), the yield strength σ_y and tensile strength σ_u of DMWJs in PWRs obtained by the continuous indentation test are illustrated in Figures 4 and 5, respectively. The yield strength displayed in Figure 4, which in the HAZ is greater than that of the base metal, reached the maximum value (689 MPa) at the FB line. Simultaneously, the yield strength fluctuated significantly in the HAZ and its adjacent regions, which reached stability at about 5 mm from the FB line. The yield stress values of the cladding metal (304 L) and base metal (SA508) are 371 MPa and 501 MPa, respectively. It is indicated that the yield strength uneven distribution within 5 mm on both sides of the FB line of
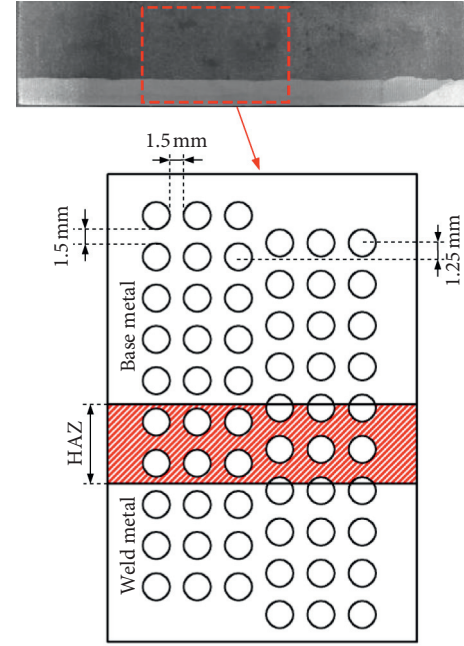

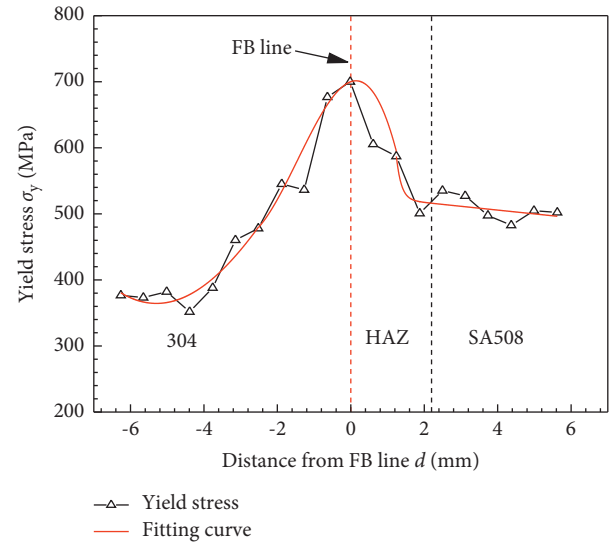FIGURE 3: The distribution diagram of the continuous indentation test point.

FIGURE 4: Local yield strength σ_y distribution of welded joints at different positions from the FB line.

DMWJs in PWRs. In addition, the yield strength decreases monotonically in the range of 2.5 mm~5 mm on both sides of the FB line, and the material at a distance of 5 mm from the FB line is homogeneous. It can be seen from Figure 5 that the tensile strength value near the FB line of DMWJs increases significantly and reaches the maximum at the position at FB line, which is similar to the yield strength distribution of DMWJs. The tensile strength value of the welded joint tends to be gentle the farther away from the FB line and reaches a stable value at about 5 mm from the FB line.
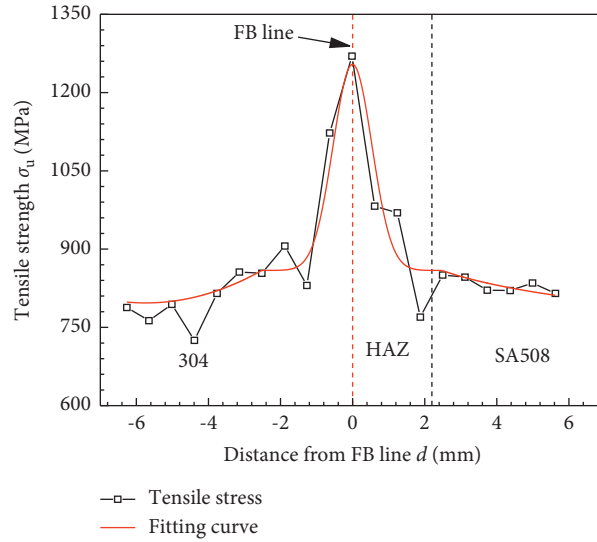
FIGURE 5: Local tensile strength σ_u distribution of welded joints at different positions from FB line.

3. Calculation Model

3.1. Geometric Model. Compact tension (CT) specimen is usually used in SCC experiments in high temperature of PWRs [14, 35]. A typical DMWJ in PWRs has a pipe inner diameter of 834.6 mm and a wall thickness of 83.5 mm. The welded joint can be simplified as a two-dimensional plane strain model when the inner diameter of the pipe is greater than the crack length ($a = 2$ mm). Because of the limitation in the size of the DMWJ in PWRs, the 0.5T-CT specimen with prefabricated crack is adopted in this numerical simulation test according to the American Society for Testing and Materials Standards [36]. Figures 6(a) and 6(b) exhibit the finite element geometric model with the transverse or longitudinal prefabricated crack, respectively, where x is the distance of the crack tip to the FB line.

3.2. FEM Model. The XFEM is different from the traditional finite element method. It requires low mesh density at the crack tip and does not need remeshing during crack propagation [29, 37]. The global grid for a specimen containing cracks is shown in Figure 7, where the crack propagates along the X-direction, and the Y-direction is the normal direction of the crack at the coordinate system. According to Mose's [38] research, the finite element size near the crack tip significantly impacts the numerical simulation results. The finite element model with 44,706 nodes of 4-node biquadratic plane strain quadrilateral (CPE4), and the element size of the crack propagation zone

is 0.08×0.08 mm. To contend the finite element model to convergence effect, 3 mm load displacement is adopted to the loading hole in Y-direction, and the velocity is 0.1 mm/s. All other motions of the center point are restrained except the vertical direction. Simultaneously, the coupling constraint was defined between the center point and the loaded hole.

3.3. Heterogeneous Material Model. Many material constitutive models have been provided to users in ABAQUS, but they are only adopted to homogeneous metals. Nevertheless, the material mechanical properties at DMWJs are heterogeneous, which has been verified by the continuous indentation test. In this research, a heterogeneous material model of the DMWJ has been established based on the USDFLD subroutine. The subroutine flowchart is shown in Figure 8, which is programmed in the FORTRAN language [39].

Firstly, the heterogeneous materials of DMWJs are related to the finite element coordinate position, and the functional relationship is established. In this research, equations (6) and (7) between the finite element X-coordinate Ux and the strength parameters (σ_y and σ_u) shown in Figures 4 and 5 are established; the strain hardening exponent n and Poisson ratio are set to constant 0.135 and 0.3, respectively. Since then, the predefined material "MAT" in the FEM model has been invoked by the state variable STATEV (x) for the field variable $f(x)$ [40].
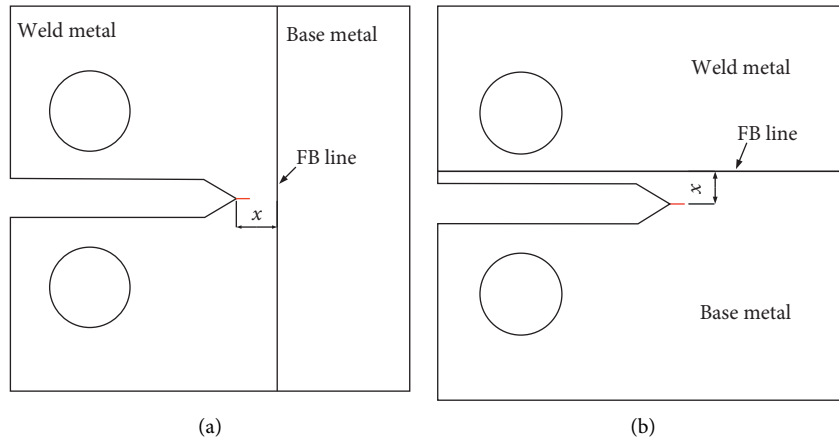
(a)

(b)

FIGURE 6: Geometrical model of 0.5T-CT specimen. (a) With a transverse crack and (b) with a longitudinal crack.
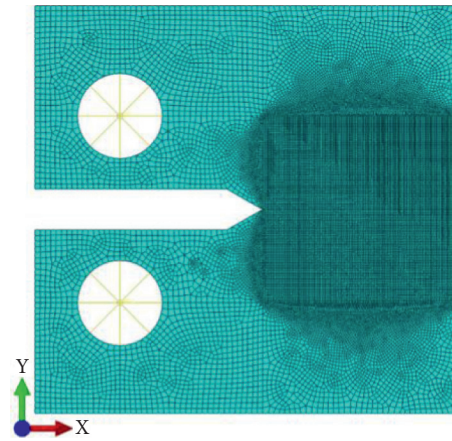

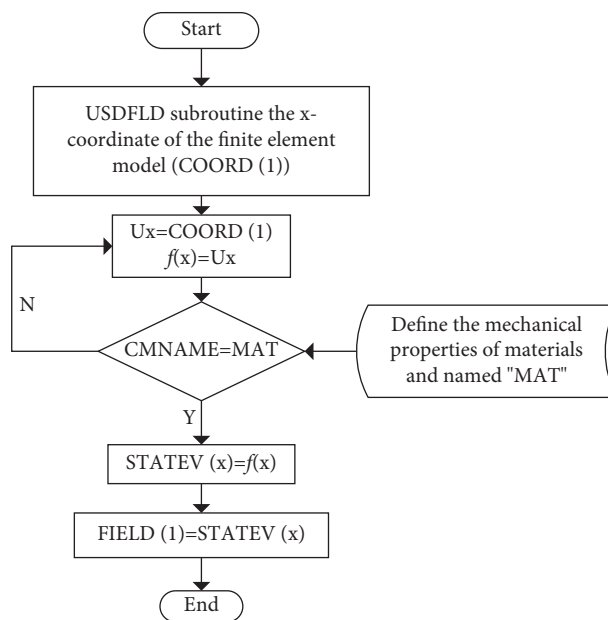FIGURE 7: The global grid model of 0.5T-CT specimen.

FIGURE 8: The flowchart of USDFLD subroutine.

$$f(\sigma_y) = \begin{cases} -14199.89732 - 18134.61098^*x - 8627.27007^*x^2 \\ -1980.46625^*x^3 - 220.81559^*x^4 - 9.61147^*x^5, & x \in [-6, -2.5], \\ 708.28507 + 72.39112^*x - 42.98274^*x^2 - 14.32451^*x^3, & x \in (-2.5, 0], \\ 693.54792 - 105.22038^*x - 21.06259^*x^2 + 14.81856^*x^3, & x \in (0, 2.5], \\ 2638.28939 - 3536.61282^*x + 2274.69416^*x^2 \\ -697.70363^*x^3 + 101.83768^*x^4 - 5.68098^*x^5, & x \in (2.5, 6], \end{cases} \tag{6}$$

$$f(\sigma_u) = \begin{cases} -2575.0118 - 3536.823^*x - 1296.90847^*x^2 \\ -199.89389^*x^3 - 11.06732^*x^4, & x \in [-6, -2.5], \\ 1278.05014 + 409.01145 * x + 82.86216^*x^2 - 5.05846^*x^3, & x \in (-2.5, 0], \\ 1249.62337 - 405.71698^*x + 91.35028^*x^2 + 1.9414^*x^3, & x \in (0, 2.5], \\ -3065.83017 + 4636.0946^*x - 2065.51854^*x^2 \\ +428.31305^*x^3 - 40.71513^*x^4 + 1.36519^*x^5, & x \in (2.5, 6]. \end{cases} \tag{7}$$

3.4. Damage Model in XFEM.

The damage model in XFEM is used to define the damage and final failure process of the simulated damage element. Its failure mechanism includes damage initial criterion and damage evolution law. When the initial damage criterion is satisfied, the damage will occur according to the defined damage evolution law.

3.4.1. Crack Initiation Criterion and Crack Propagation Direction.

The stress intensity factor K is the criterion of crack initiation when dealing with the numerical simulation of the crack initiation of the DMWJ in PWRs. The crack will initiate propagation behavior until the stress intensity factor reaches the threshold value K_{IC}. Since the stress intensity factor is mainly determined by the maximum principal stress at the crack tip, the maximum principal stress is selected as the initiation criterion in the XFEM damage model [37, 39].

$$f = \left\{ \frac{\langle \sigma_{max} \rangle}{\sigma_{max}^0} \right\}, \tag{8}$$

where σ_0 max is critical maximum principal stress, σ_{max} is the maximum principal stress, the Macaulay brackets $\langle \rangle$ is used to indicate that the pure compressive stress state is not initial damage, and f is a fracture criterion based on the ratio of the maximum principal stress; it will cause crack initiation when $f > 1$. In this research, the crack is Model I, and the maximum principal stress equals the tensile strength. The tensile strength uneven distribution of DMWJ in the heterogeneous material model is shown in Figure 6.

3.4.2. Damage Evolution Law.

The crack propagation is determined by calculating whether the equivalent strain energy release rate G_{equiv} reaches the critical equivalent strain energy release rate G_{equivC}. Moreover, the critical equivalent strain energy release rates G_{IC}, G_{IIC}, and G_{IIIC} reflect the fracture resistance of materials during crack propagation. The power law based on energy is involved in this research to the crack propagation after the crack initiates.

$$\frac{G_{equiv}}{G_{equivC}} = \left(\frac{G_I}{G_{IC}} \right)^{a_m} + \left(\frac{G_{II}}{G_{IIC}} \right)^{a_n} + \left(\frac{G_{III}}{G_{IIIC}} \right)^{a_o}, \tag{9}$$

where a_m, a_n, and a_o are damage exponents. In this research, the crack is Model I, so only the first item in equation (9) is adopted. According to Irwin [41], the plastic energy and crack surface energy of material loss are constant during crack propagation, and the critical energy release rate reflects the fracture resistance of material during crack propagation.

$$G = -\frac{d\Pi}{dA} = -\lim_{\Delta A \longrightarrow 0} \frac{\Delta \Pi}{\Delta A} = -\lim_{\Delta A \longrightarrow 0} \frac{\Delta \Pi}{B \Delta a}, \tag{10}$$

where ΔA is crack surface area; $\Pi = U - W$ is potential energy, U is strain energy of the crack and W is external work; B is the crack width; and a is the crack length. Yang et al. [29] adopted the virtual crack closure technique (VCCT) with two steps for obviously the fracture energy release rate G:

$$G \approx \frac{\Pi_2 - \Pi_1}{B \Delta a}, \tag{11}$$

where Π_2 and Π_1 are the potential energy in steps 2 and 1, respectively.

4. Results and Discussion

Based on the heterogeneous material model, the crack propagation behavior in DMWJ specimens with prefabricated transverse and longitudinal cracks was discussed by the elastic-plastic extension finite element method.

4.1. The Propagation Path of Transverse Crack.

Figure 9 shows the crack propagation paths and tensile stress distribution of the transverse crack, where the crack propagation does not deviate from the initiation direction. It illustrated that the crack propagation does not occur the deflection propagation behavior when the crack propagation direction is consistent with the change direction of mechanical properties, which has been identified in the previous literature. Some studies indicated that although the FB line hinders crack propagation, the crack will propagate
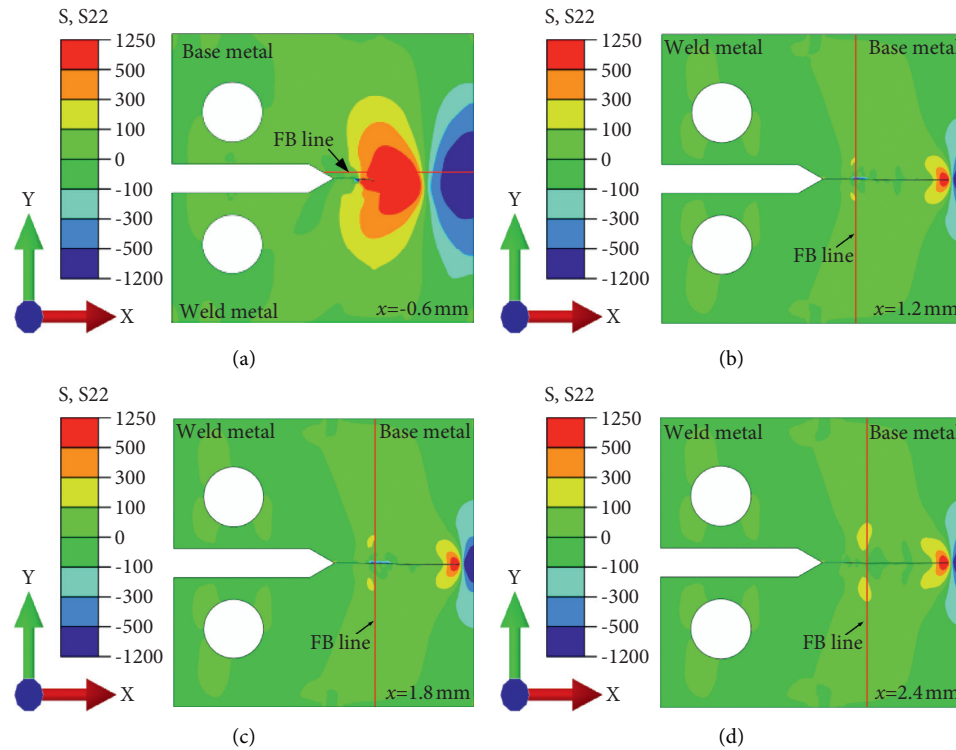
FIGURE 9: Crack extension path and tensile stress distribution of transverse cracks: (a) $x = 0.6$, (b) $x = 1.2$, (c) $x = 1.8$, and (d) $x = 2.4$.

through the FB line and continue to propagate along the initiation direction [4, 42]. In addition, the large tensile stress concentration at the crack tip and the specimen boundary along the crack front were subjected to compressive stress.

The length of the crack propagation varies with the loading hole displacement load on the CT specimen as shown in Figure 10, which can be seen that the crack propagation length is the same when the initial crack tip is 1.2 mm, 1.8 mm, and 2.4 mm away from the FB line, and the minimum is when the distance is 0.6 mm. It indicated that the crack propagation length is smaller as the initial transverse crack tip is closer to the FB line under the same load condition. The transverse crack propagation to the FB line in Figure 10 has been marked with black symbols, which demonstrates that the crack propagation behavior in DMWJs would continue to propagate through the FB line in the PWRs. Some previous studies have revealed that the crack gradually propagates through the FB line and the dilution zone (DZ) of the base metal after initiation [2, 43, 44].

They are combined with the local strength distribution of DMWJs in PWRs as shown in Figures 4 and 5, where the strength (yield strength σ_y and tensile strength σ_u) at the FB line is the largest. Therefore, the numerical simulation results show that the transverse crack could propagate from low to high strength region and continue to propagate to the low strength zone after growth through the highest strength zone, which has been identified in the previous literature. Seifert et al. proposed that the SCC in weld metal very easily crossed the fusion line and further propagated with a high
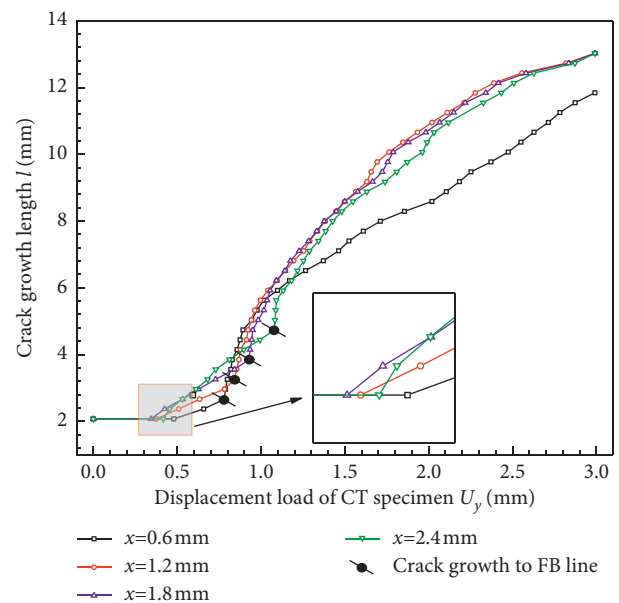

FIGURE 10: The crack propagation length curves with the displacement load.

growth rate as a transgranular crack into the heat-affected zone and base material of the adjacent low-alloy steel [45].

It should be noticed that the crack propagation length l in DMWJs varies significantly with unit displacement load (U_y) in the near zone of the FB line from Figure 10. To characterize the variation of crack growth length with displacement load in detail, the slope of the four curves

($k = \Delta l/\Delta U_y$) shown in Figure 10 is set to crack growth length under unit displacement load. Figure 11 shows the variation of crack propagation length with unit-load displacement, where the value of k changes dramatically near the FB line. Combining with the strength distribution of DMWJs in PWRs as shown in Figures 4 and 5, the crack growth length of unit load displacement is relatively small before reaching the FB line and the crack propagation from low to high strength in this region. Previous studies have revealed that the FB line hinders crack growth perpendicular to the FB line, most likely because the complex stress-strain field at crack tip and oxidation along the FB increase the crack growth distance [7, 43, 46]. Conversely, the crack propagation length suddenly increases when the crack crosses the FB line, and then the crack propagates from the high to low strength region. It demonstrated that the crack propagation length is mainly affected by the uneven distribution of the strength in the DMWJ. It changes suddenly when the crack propagates to the FB line, and it is sustained changes on both sides of the FB line.

4.2. The Mechanical Characteristic at the Transverse Crack Tip.
Previous studies have shown that the stress-strain condition at the crack tip is one of the main factors affecting the crack propagation behavior. It can be seen from the local amplification diagram in Figure 10 that the displacement loads are different at the crack initiation point when the initial crack is at a different distance from the FB line. Simultaneously, it is shown in Figure 11 that the crack propagation length (k) is also different at the crack initiation point. Therefore, the Mises stress σ_m and equivalent plastic strain ε_{eq} curves at the tip of the transverse cracks are investigated in this research.

Figure 12 shows the Mises stress σ_m curves of 0.2 mm in front of transverse cracks, which indicates that the Mises stress decreases with the increase of the distance from the crack tip. The Mises stress is the largest when the transverse crack tip is 0.6 mm from the FB line, which indicates that the closer the transverse crack is to the fusion line, the larger stress is required for the crack initiation behavior. It means that the closer the transverse crack from the FB line, the more difficult it is to initiate behavior under the same load conditions.

The equivalent plastic strain ε_{eq} curves at the crack tip front of the transverse cracks are shown in Figure 13, where the value curves are the largest when the transverse crack tip is 0.6 mm from the FB line. The equivalent plastic strain curves coincided with the transverse crack tips 1.2 mm and 1.8 mm away from the FB line. The distribution of the equivalent plastic strain curves in Figure 13 is consistent with the displacement of the crack initiation behavior in Figure 10. It can be seen that the larger the equivalent plastic strain at the front of the transverse crack, the larger the displacement load of the crack initiation behavior.

The previous section mentioned that the transverse crack in weld metal would continue to propagate in the base metal through the FB line. The stress-strain condition is concerned by many scholars when the crack propagates to the FB line.
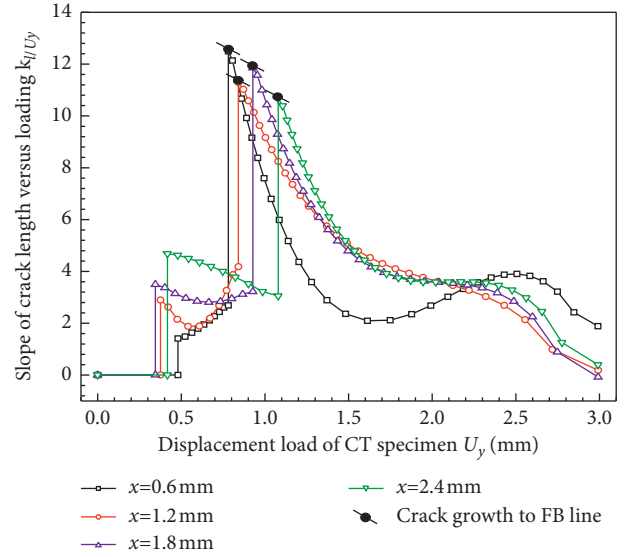

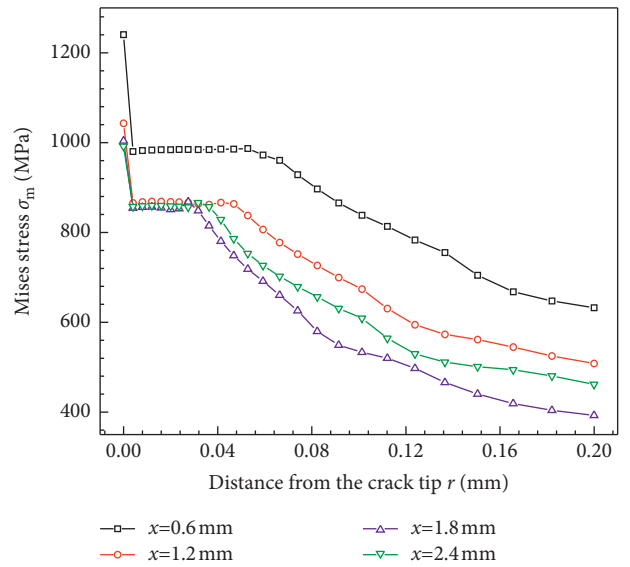FIGURE 11: The crack propagation length with unit-load displacement curves.

FIGURE 12: Mises stress curves at the front of initiation crack tip.

Figure 14 illustrates the Mises stress σ_m curves of 0.2 mm in front of transverse cracks when the crack propagates to the FB line, where the Mises stress decreases with the distance from the crack tip. It can be seen from Figure 14 that the Mises stress at the crack tip front increases with the increasing length of the initial transverse cracks distance from the FB line. It indicates that a larger driving force is required for crack propagation behavior when the crack propagates to the FB line. It also verifies the conclusions of previous studies that the FB line hinders crack growth [43, 47].

Figure 15 illustrates the equivalent plastic strain ε_{eq} curves in front of transverse cracks when the crack propagates to the FB line. The equivalent plastic strain ε_{eq} value is larger when the initial transverse crack is closer to the FB
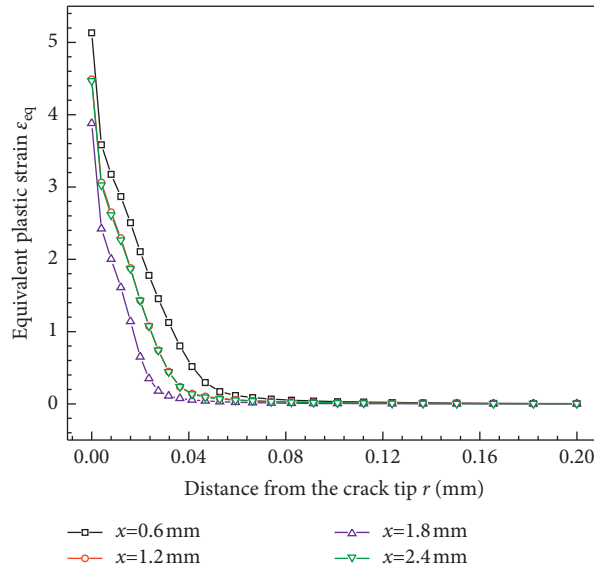
FIGURE 13: Equivalent plastic strain curves at the front of initiation crack tip.
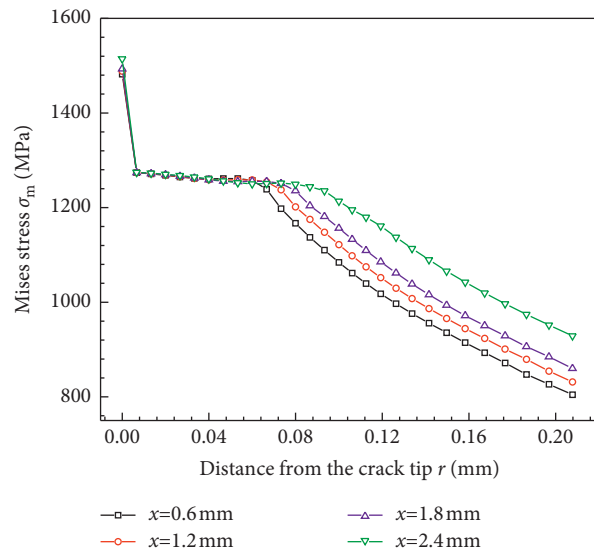

FIGURE 14: Mises stress curves at the front of FB line crack tip.

line. The distribution of the equivalent plastic strain curves in Figure 15 is consistent with the displacement of the transverse crack propagation to the FB line in Figure 10. It can be seen that the displacement load is larger when cracks are propagated to the FB line and the equivalent plastic strain value is larger at the transverse crack front.

4.3. The Propagation Path of Longitudinal Crack. The crack propagation path and tensile stress distribution of the longitudinal cracks are shown in Figure 16, where the initial crack propagation is along the X-direction. Nevertheless, the material mechanical properties change along the Y-direction, which is perpendicular to the crack propagation direction. The extension path of longitudinal

cracks in the weld metal is shown in Figures 16(a)–16(c). It can be seen that the longitudinal cracks in weld metal deflect away from the FB line. In addition, the longitudinal cracks in base metal deflect away from the FB line, as shown in Figures 16(d)–16(f). Previous researches have focused on the effect of the strength mismatch on the crack propagation path, and the results indicated that the crack tends to deflect along the low yield strength side [29, 48].

Extract the longitudinal crack extension paths in the two-dimensional plane as shown in Figure 17, where the longitudinal cracks in the DMWJ will deviate from the initial crack direction and propagate along the direction away from the FB line. It indicates that the noninterface cracks in DMWJs do not propagate through the FB line. Combined
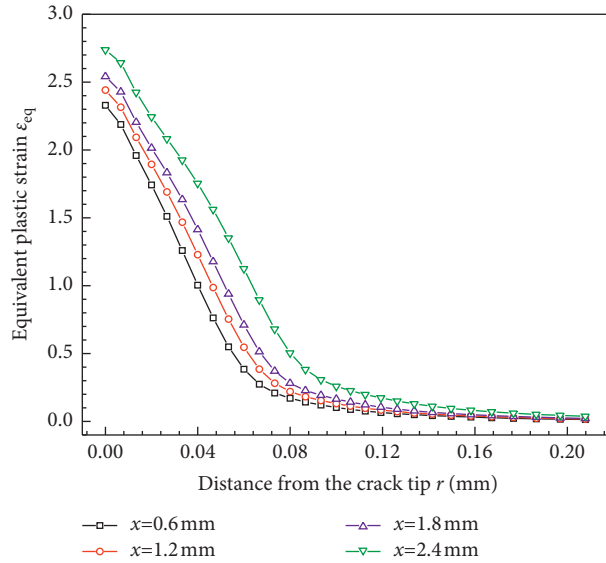
FIGURE 15: Equivalent plastic strain curves at the front of FB line crack tip.
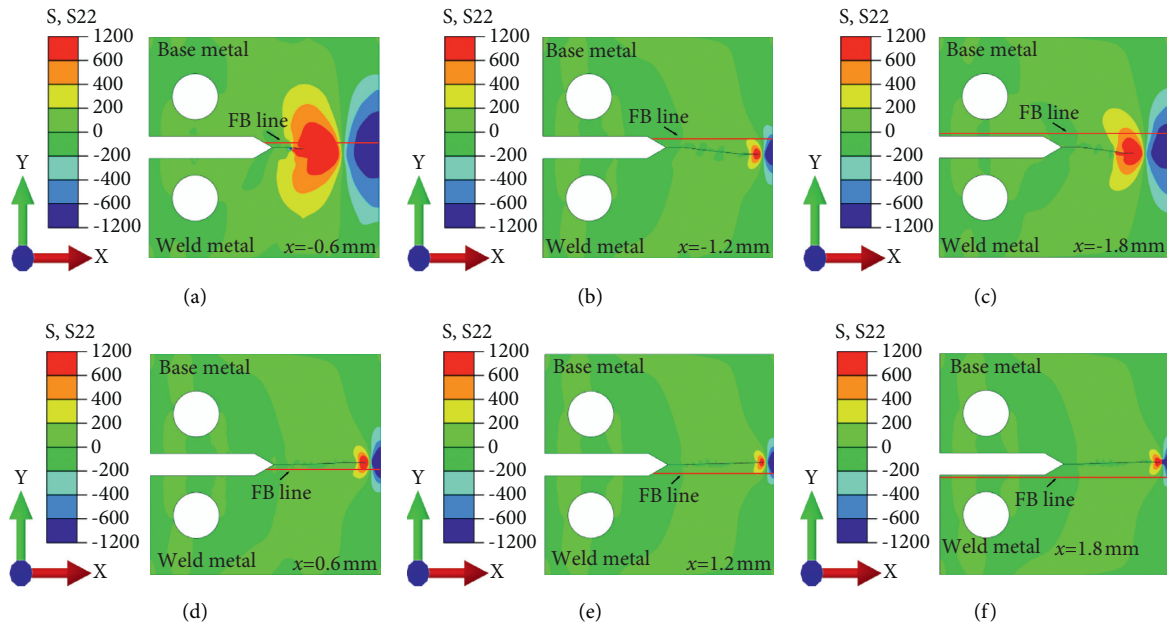

FIGURE 16: Crack extension paths and tensile stress distribution of longitudinal cracks: (a) $x = -0.6$, (b) $x = -1.2$, (c) $x = -1.8$, (d) $x = 0.6$, (e) $x = 1.2$, and (f) $x = 1.8$.

with the strength distribution of DMWJs shown in Figures 4 and 5, the yield strength and tensile strength decreased gradually on both sides of the FB line, since the longitudinal cracks in the welded joints will deflect along the side with smaller strength. In addition, the yield strength at the FB line is 188 MPa larger than that of base metal (SA508) and 318 MPa larger than that of weld metal (304 L) in Figure 4; the deflection amplitude of longitudinal cracks in weld metal was larger than that in base metal. It indicated that the uneven distribution of yield strength in DMWJs is one of the main factors affecting the deflection amplitude of crack propagation. It is also worth noticing in Figure 17 that the
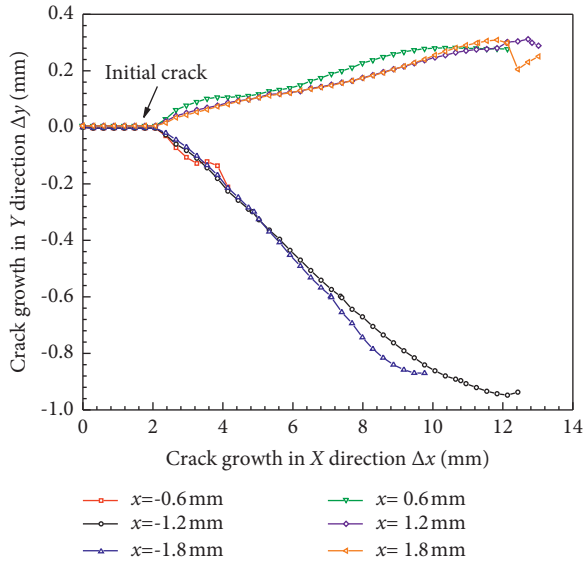
Figure 17: Crack extension paths of longitudinal cracks.

crack extension length is smaller as the noninterface crack is closer to the FB line under the same displacement load condition.

5. Conclusions

The main acquired results are summarized as follows:

(1) The mechanical properties of DMWJ were obtained by the continuous ball indentation test. The results indicated that the strength value at the FB line reaches a maximum, and the yield strength maximum is 689 MPa. The region of 5 mm from the FB line can be considered homogeneous metal, and the yield stress values of the cladding metal (304 L) and base metal (SA508) are 371 MPa and 501 MPa, respectively.

(2) When the initial transverse cracks are perpendicular to the FB line, the transverse crack propagates through the FB line, and the crack propagation does not deviate from the initial direction. At the initiation point, the stress and strain values at the tip of the transverse crack are larger as the initial crack is closer to the FB line. Conversely, the stress and strain values at the tip of transverse cracks are smaller when the crack propagates to the FB line.

(3) Since the uneven distribution of material properties of DMWJs in PWRs, the crack growth length with displacement load will change dramatically at the FB line. The crack growth length is released and increases suddenly when the crack extension through the FB line from the weld metal to the base metal region, and the rate gradually decreases in the base metal region.

(4) When the initial longitudinal cracks parallel the FB line, the propagation of the longitudinal cracks will deviate from the initial direction. The initial longitudinal crack is located in the base metal or weld metal, and the crack will deviate away from the FB line. In addition, the crack propagation length is smaller as the noninterface crack is closer to the FB line under the same load conditions.

Data Availability

The mechanical property parameters of welded joints were obtained based on continuous ball indentation tests, which were used to support the findings of this study are included within the article.

Conflicts of Interest

The authors declare that they have no conflicts of interest.

Acknowledgments

References

[1] H. Ming, Z. Zhang, J. Wang, and E.-H. Han, "Microstructure of a domestically fabricated dissimilar metal weld joint (SA508-52M-309L-CF8A) in nuclear power plant," *Materials Characterization*, vol. 148, pp. 100–115, 2019.

[2] L. Dong, Q. Peng, H. Xue, E.-H. Han, W. Ke, and L. Wang, "Correlation of microstructure and stress corrosion cracking initiation behaviour of the fusion boundary region in a SA508 Cl. 3-Alloy 52 M dissimilar weld joint in primary pressurized water reactor environment," *Corrosion Science*, vol. 132, pp. 9–20, 2018.

[3] H. Ming, R. Zhu, Z. Zhang et al., "Microstructure, local mechanical properties and stress corrosion cracking susceptibility of an SA508-52M-316LN safe-end dissimilar metal weld joint by GTAW," *Materials Science and Engineering: A*, vol. 669, pp. 279–290, 2016.

[4] J. Hou, Q. Peng, Y. Takeda, J. Kuniya, and T. Shoji, "Microstructure and stress corrosion cracking of the fusion boundary region in an alloy 182-A533B low alloy steel dissimilar weld joint," *Corrosion Science*, vol. 52, no. 12, pp. 3949–3954, 2010.

[5] S. Kumar, V. K. Yadav, S. K. Sharma, C. Pandey, A. Goyal, and P. Kumar, "Role of dissimilar Ni-based ERNiCrMo-3 filler on the microstructure, mechanical properties and weld induced residual stresses of the ferritic/martensitic P91 steel welds joint," *International Journal of Pressure Vessels and Piping*, vol. 193, Article ID 104443, 2021.

[6] J. Wang, T. Zhu, Y. Han et al., "Environment assisted cracking of 308L weld metal in high temperature water," *Journal of Nuclear Materials*, vol. 557, Article ID 153275, 2021.

[7] L. Dong, Y. Zhang, Y. Han, Q. Peng, and E. H. Han, "Environmentally assisted cracking in the fusion boundary region of a SA508-Alloy 52 M dissimilar weld joint in simulated primary pressurized water reactor environments," *Corrosion Science*, vol. 190, Article ID 109668, 2021.

[8] L. Dong, E.-H. Han, Q. Peng, W. Ke, and L. Wang, "Environmentally assisted crack growth in 308 L stainless steel weld metal in simulated primary water," *Corrosion Science*, vol. 117, pp. 1–10, 2017.

[9] W. Bamford, B. Newton, and D. Seeger, "Recent experience with weld overlay repair of indications in alloy 182 butt welds in two operating PWRs," in *Proceedings of the ASME Pressure Vessels and Piping Conference*, pp. 427–434, Vancoucer, BC, Canada, July 2006.

[10] K. W. Fang, G. J. Li, G. F. Li, W. Yang, M. L. Zhang, and Z. Y. Sun, "Microstructures and mechanical properties of dissimilar metal weld A508/52M/316L used in nuclear power plants," *Key Engineering Materials*, vol. 479, pp. 40–47, 2011.

[11] H. T. Wang, G. Z. Wang, F. Z. Xuan, C. J. Liu, and S. T. Tu, "Local mechanical properties of a dissimilar metal welded joint in nuclear power systems," *Materials Science and Engineering: A*, vol. 568, pp. 108–117, 2013.

[12] H. T. Wang, G. Z. Wang, F. Z. Xuan, C. J. Liu, and S. T. Tu, "Local mechanical properties and microstructures of Alloy 52 M dissimilar metal welded joint between A508 ferritic steel and 316 L stainless steel," *Advanced Materials Research*, vol. 509, pp. 103–110, 2012.

[13] J. Zhang, Y. Huang, D. Fan et al., "Microstructure and performances of dissimilar joints between 12Cr2Mo1R steel and 06Cr18Ni11Ti austenitic stainless steel joined by AA-TIG welding," *Journal of Manufacturing Processes*, vol. 60, pp. 96–106, 2020.

[14] H. Xue, K. Ogawa, and T. Shoji, "Effect of welded mechanical heterogeneity on local stress and strain ahead of stationary and growing crack tips," *Nuclear Engineering and Design*, vol. 239, no. 4, pp. 628–640, 2009.

[15] L. Zhao, H. Xue, W. Tang, and X. Fang, "Effect of welded mechanical heterogeneity on local stress and strain ahead of growing crack tips in the piping welds," in *Proceedings of the Pressure Vessels and Piping Conference*, pp. 223–232, Baltimore, MD, USA, July 2011.

[16] H. Xue, Z. Li, Z. Lu, and T. Shoji, "The effect of a single tensile overload on stress corrosion cracking growth of stainless steel in a light water reactor environment," *Nuclear Engineering and Design*, vol. 241, no. 3, pp. 731–738, 2011.

[17] A. Sauraw, A. K. Sharma, D. Fydrych et al., "Study on microstructural characterization, mechanical properties and residual stress of GTAW dissimilar joints of P91 and P22 steels," *Materials*, vol. 14, no. 21, p. 6591, 2021.

[18] G. Rogalski, A. Świerczyńska, M. Landowski, and D. Fydrych, "Mechanical and microstructural characterization of TIG welded dissimilar joints between 304 L austenitic stainless steel and Incoloy 800HT nickel alloy," *Metals*, vol. 10, no. 5, Article ID 559, 2020.

[19] S. Shuqian, C. Lixun, C. Hui, B. Chen, and L. Xiaokun, "Theoretical model and testing method for ball indentation based on the proportional superposition of energy in pure elasticity and pure plasticity," *Chinese Journal of Aeronautics*, vol. 35, no. 2, pp. 141–153, 2021.

[20] H. Xue, J. He, W. Jia et al., "An approach for obtaining mechanical property of austenitic stainless steel by using continuous indentation test analysis," *Structures*, vol. 28, pp. 2752–2759, 2020.

[21] P. Phani, W. Oliver, and G. M. Pharr, "Measurement of hardness and elastic modulus by load and depth sensing indentation: improvements to the technique based on continuous stiffness measurement," *Journal of Materials Research*, vol. 36, pp. 2137–2153, 2021.

[22] B. Zou, K. S. Guan, and S. B. Wu, "Determination of area reduction rate by continuous ball indentation test," *International Journal of Pressure Vessels and Piping*, vol. 139-140, pp. 220–227, 2016.

[23] Y. Yang, W. Q. Wang, and M. D. Song, "The measurement of mechanical properties of pipe steels in service through continuous ball indentation test," *Procedia Engineering*, vol. 130, pp. 1742–1754, 2015.

[24] F. Q. Yang, H. Xue, L. Y. Zhao, and X. R. Fang, "A quantitative prediction model of SCC rate for nuclear structure materials in high temperature water based on crack tip creep strain rate," *Nuclear Engineering and Design*, vol. 278, pp. 686–692, 2014.

[25] G. Wang, H. Wang, F. Xuan, S. Tu, and C. Liu, "Local fracture properties and dissimilar weld integrity in nuclear power plants," *Frontiers of Mechanical Engineering*, vol. 8, no. 3, pp. 283–290, 2013.

[26] H. T. Wang, G. Z. Wang, F. Z. Xuan, and S. T. Tu, "An experimental investigation of local fracture resistance and crack growth paths in a dissimilar metal welded joint," *Materials & Design*, vol. 44, pp. 179–189, 2013.

[27] K. Fan, G. Z. Wang, F. Z. Xuan, and S. T. Tu, "Effects of work hardening mismatch on fracture resistance behavior of bi-material interface regions," *Materials & Design*, vol. 68, pp. 186–194, 2015.

[28] K. Fan, G. Z. Wang, F. Z. Xuan, and S. T. Tu, "Local failure behavior of a dissimilar metal interface region with mechanical heterogeneity," *Engineering Failure Analysis*, vol. 59, pp. 419–433, 2016.

[29] F. Q. Yang, H. Xue, L. Y. Zhao, and X.-R. Fang, "Effects of welded mechanical heterogeneity on interface crack propagation in dissimilar weld joints," *Advances in Materials Science and Engineering*, vol. 2019, Article ID 6593982, 10 pages, 2019.

[30] D. Tabor, *The Hardness of Metals*, Oxford University Press, Oxford, UK, 2000.

[31] Y. Li, P. Stevens, M. Sun, C. Zhang, and W. Wang, "Improvement of predicting mechanical properties from spherical indentation test," *International Journal of Mechanical Sciences*, vol. 117, pp. 182–196, 2016.

[32] ISO, NPR-ISO/TR 29381, metallic materials-measurement of mechanical properties by an instrumented indentation test—indentation tensile properties (ISO/TR 29381: 2008, IDT).

[33] J.-H. Ahn and D. Kwon, "Derivation of plastic stress-strain relationship from ball indentations: examination of strain definition and pileup effect," *Journal of Materials Research*, vol. 16, no. 11, pp. 3170–3178, 2001.

[34] M. Dao, N. Chollacoop, K. J. Van Vliet, T. A. Venkatesh, and S. Suresh, "Computational modeling of the forward and reverse problems in instrumented sharp indentation," *Acta Materialia*, vol. 49, no. 19, pp. 3899–3918, 2001.

[35] R. Zhu, J. Wang, Z. Zhang, and E.-H. Han, "Stress corrosion cracking of fusion boundary for 316L/52M dissimilar metal weld joints in borated and lithiated high temperature water," *Corrosion Science*, vol. 120, pp. 219–230, 2017.

[36] Astm Standard E399-90, "Standard test method for plane strain fracture toughness of metallic materials," in *Annual Book of ASTM Standards*American Society for Testing Materials, West Conshohocken, PA, USA, 2002.

[37] Q. Z. Xiao and B. L. Karihaloo, "Improving the accuracy of XFEM crack tip fields using higher order quadrature and statically admissible stress recovery," *International Journal for Numerical Methods in Engineering*, vol. 66, no. 9, pp. 1378–1410, 2006.

[38] P. Rozycki, N. Moes, E. Bechet, and C. Dubois, "X-FEM explicit dynamics for constant strain elements to alleviate mesh constraints on internal or external boundaries,"

Computer Methods in Applied Mechanics and Engineering, vol. 197, no. 5, pp. 349–363, 2008.

[39] Dassault Systèmes Simulia Corp, *ABAQUS, Version 6.14 Documentation*, Dassault Systèmes Simulia Corp, Providence, RI, USA, 2014.

[40] X. Wang, B. Zhang, S. Du, Y. Wu, and X. Sun, "Numerical simulation of the fiber fragmentation process in single-fiber composites," *Materials and Design*, vol. 31, no. 5, pp. 2464–2470, 2010.

[41] G. R. Irwin, "Fracture," in *Handbuch der Physik*, S. Flugge, Ed., pp. 551–590, Springer, Berlin, Germany, 1958.

[42] B. Alexandreanu, Y. Chen, W. Y. Chen, and K. Natesan, "Stress corrosion cracking of alloy 52/152 weldments near dissimilar metal weld interfaces," in *Proceedings of the 18th International Conference on Environmental Degradation of Materials in Nuclear Power Systems–Water Reactors*, pp. 67–85, Portland, OR, USA, August 2017.

[43] H. P. Seifert, S. Ritter, T. Shoji, Q. J. Peng, Y. Takeda, and Z. P. Lu, "Environmentally-assisted cracking behaviour in the transition region of an Alloy182/SA 508 Cl.2 dissimilar metal weld joint in simulated boiling water reactor normal water chemistry environment," *Journal of Nuclear Materials*, vol. 378, no. 2, pp. 197–210, 2008.

[44] H. Ming, J. Wang, and E.-H. Han, "Comparative study of microstructure and properties of low-alloy-steel/nickel-based-alloy interfaces in dissimilar metal weld joints prepared by different GTAW methods," *Materials Characterization*, vol. 139, pp. 186–196, 2018.

[45] H.-P. Seifert, S. Ritter, H. J. Leber, and S. Roychowdhury, "Stress corrosion cracking behavior in the transition region of alloy 182/low-alloy reactor pressure vessel steel dissimilar metal weld joints in light water reactor environments," *Corrosion*, vol. 71, no. 4, pp. 433–454, 2015.

[46] Q. Peng, H. Xue, J. Hou, Y. Takeda, J. Kuniya, and T. Shoji, "Stress corrosion cracking in the fusion boundary region of an alloy 182-A533B low alloy steel dissimilar weld joint in high temperature oxygenated water," 2011.

[47] Q. Peng, H. Xue, J. Hou et al., "Role of water chemistry and microstructure in stress corrosion cracking in the fusion boundary region of an Alloy 182-A533B low alloy steel dissimilar weld joint in high temperature water," *Corrosion Science*, vol. 53, no. 12, pp. 4309–4317, 2011.

[48] Y. Bi, X. Yuan, J. Lv et al., "Effect of yield strength distribution welded joint on crack propagation path and crack mechanical tip field," *Materials*, vol. 14, no. 17, Article ID 4947, 2021.